*Inorg. Chem.* **2007**, *46*, 2057–2066


# Second-Sphere Ligand-Field Effects in Solid Solutions of Anhydrous Transition-Metal Phosphates

**H. Thauern[†] and R. Glaum***

*Department of Inorganic Chemistry, University of Bonn, Gerhard-Domagk-Strasse 1, D-53121 Bonn, Germany*

Received August 7, 2006

Powders of the solid solutions $In_{1-x}Cr_xPO_4$ ($0 \le x \le 1$), $In_{1-x}Cr_x(PO_3)_3$ ($0 \le x \le 1$), $(In_{1-x}Cr_x)_4(P_2O_7)_3$ ($0 \le x \le 0.7$), and $In_{1-x}Mn_x(PO_3)_3$ ($0 \le x \le 0.8$) have been synthesized by solid-state reactions. Depending on the dopant concentration, these materials show striking variations in color [$In_{1-x}Cr_xPO_4$, light pink to green-brown; $(In_{1-x}Cr_x)_4(P_2O_7)_3$, light pink to red-brown; $In_{1-x}Cr_x(PO_3)_3$, pale green to green; $In_{1-x}Mn_x(PO_3)_3$, light blue to purple). Powder reflectance spectra of the solid solutions were measured in the UV/vis/NIR region (5500–35000 $cm^{-1}$). Observed d–d electronic transition energies and results of calculations within the framework of the angular overlap model (AOM) for the low-symmetry chromophores [$M^{III}O_6$] (M = Cr, Mn) are in good agreement. In the case of the mixed In/Cr phosphates, the observed color changes can be related to second-sphere ligand-field effects. Clear evidence for differences in the $\pi$-bonding of oxygen toward $Cr^{3+}$ ($d^3$ ion) and $In^{3+}$ ($d^{10}$ ion) are observed. For $In_{1-x}Mn_x(PO_3)_3$, the variation in color is attributed to a slightly increasing elongation of the [$Mn^{III}O_6$] chromophore with increasing dopant concentration.

## Introduction

$Cr_2O_3$ and $Ca_3Cr_2Si_3O_{12}$[2] are well-known green pigments; chromium(III)-doped alumina and some spinels are commercially used pink pigments. A disadvantage of the latter is a generally rather low color saturation, preventing their application as red pigments. Further interest in thermally very stable red chromium oxo-compounds has been triggered by the search for new, improved laser materials as substitutes for ruby.[3] We started our studies on the color of transition-metal oxo-compounds (with emphasis on anhydrous phosphates) to gain new insights into the correlation between the crystal-chemical properties of a chromophore and the color it lends to a solid. The analysis of the influence of low-symmetry coordination and second-sphere ligand-field effects[4] (in particular, anisotropic $\pi$-bonding of oxygen to metal ions[5]) was of special interest to our work. Therefore, we have undertaken a detailed UV/vis/NIR spectroscopic investigation of $Cr^{3+}$ and $Mn^{3+}$ doped into indium(III) phosphates. In addition to recently published results from investigations of the color of chromium oxo-compounds, where ideal octahedra were assumed in a classical ligand-field treatment,[6] we also allow for the low symmetry of the actually present chromophore.

The energies of the d−d electronic absorption bands, and hence the color of an oxide material, are determined by several effects. Well investigated are geometric influences [distances $d$(M−O) and the angular distortion] on the ligand-field splitting and the symmetry of a chromophore. Similarly well understood is the influence of the interelectronic repulsion parameters. In contrast, variations in the d−p $\pi$-interaction between the transition-metal and oxygen are far less understood. Only in recent years has experimental evidence for such an interaction and its variation been gathered and interpreted systematically.[4,5,7] To examine the various color-determining effects in greater detail, indium

* To whom correspondence should be addressed. E-mail: rglaum@uni-bonn.de. Fax: +49 228 73 56 60.

† Part of the Ph.D. Thesis of H. Thauern, University of Bonn, Bonn, Germany, 2006. URL: http://hss.ulb.uni-bonn.de/diss_online/math_nat_fak/2006/thauern_henrike/index.htm.

(1) Omitted in proof.
(2) Carda, J.; Monros, G.; Tena, M. A.; Marti, M. C.; Cordoncillo, E.; Escribano, P.; Alarcon, J. *Bol. Soc. Esp. Ceram. Vidrio* **1992**, *31*, 19.
(3) Payne, S. A.; Chase, L. L.; Wilke, G. D. *J. Lumin.* **1989**, *44*, 167.
(4) Reinen, D.; Atanasov, M.; Lee, S.-L. *Coord. Chem. Rev.* **1998**, *175*, 91.
(5) Glaum, R.; Hitchman, M. *Aust. J. Chem.* **1996**, *49*, 1221.
(6) Pavlov, R. S.; Marzá, V. B.; Carda, J. B. *J. Mater. Chem.* **2002**, *12*, 2825.
(7) Glaum, R. *Neue Untersuchungen an wasserfreien Phosphaten der Übergangsmetalle*; Thesis of Habilitation, University of Giessen, Giessen, Germany, 1999; available at http://bibd.uni-giessen.de/ghtm/1999/uni/h990001.htm (in German).

10.1021/ic061481b CCC: $37.00 
Published on Web 02/22/2007

phosphates doped with chromium or manganese are suitable compounds. The first reason for choosing these systems is provided by the different chromophore geometries in these structures. $In(PO_3)_3$[8] contains $[In^{III}O_6]$ octahedra that are isolated from each other. $In_4(P_2O_7)_3$[9] exhibits face-sharing pairs of $[In^{III}_2O_9]$ octahedra, with a symmetry close to $C_{3v}$, and $InPO_4$[10] shows chains of edge-sharing $[In^{III}O_2O_{4/2}]$ octahedra with $D_{2h}$ symmetry. Second, the host lattices were chosen because of the $d^{10}$ electron-configuration of $In^{3+}$, where, in contrast to 3d metal ions, $\pi$-interactions between the completely filled 3d orbitals of $In^{3+}$ and the p-orbitals of oxygen is impossible.

As earlier investigations have shown, $\pi$-bonding interactions between oxygen and ions with $d^0$ or $d^{10}$ electron configurations differ remarkably,[11] leading to wide variations of $\Delta_O$ in tri-rutiles $A_2NiMO_6$ (A = Ca, Sr, Ba, Y, La; M = Mg, Ti, Nb, Ta, W, U, Ge, Sn, Sb, Te). In addition, anisotropic $\pi$-bonding effects are expected to lower the symmetry of a chromophore.

It is the aim of our study to extend the knowledge on parameters determining coloration of chromium-doped solids, thus allowing a more systematic search for new color pigments and even laser materials. Our article also addresses the question of how bonding between the transition-metal ions $Cr^{3+}$ and $Mn^{3+}$ and their coordination sphere is modified upon substitution by $In^{3+}$.

## Experimental Section

**Synthesis.** Microcrystalline samples of solid solutions of the indium(III) chromium(III) phosphates $In_{1-x}Cr_xPO_4$, $In_{1-x}Cr_x(PO_3)_3$, and $(In_{1-x}Cr_x)_4(P_2O_7)_3$ were synthesized from the elements (Chem-Pur 99.99%) and dilute phosphoric acid (Merck p.a.) using the following general procedure: Elemental chromium was dissolved in dilute hydrochloric acid; the solution was then evaporated to dryness and dissolved in dilute nitric acid three times until the solution was free of chloride. Direct dissolution of chromium in dilute nitric acid turned out to be impossible because of passivation of the metal. Subsequently, elemental indium was added to the acidic solution, followed by a stoichiometric amount of dilute phosphoric acid ($c$ = 1.00 mol/L). This mixture was again evaporated ($T \approx 573$ K) to dryness. The obtained residue was then slowly heated to 1173 K in a silica crucible in air and kept at this temperature for 3 days. Thus, microcrystalline powders were obtained.

Microcrystalline samples of the solid solution $In_{1-x}Mn_x(PO_3)_3$ were prepared by dissolving both metals in dilute nitric acid, adding the appropriate amount of phosphoric acid, and evaporating the mixture to dryness. Because of the lower thermal stability of manganese(III) compared to chromium(III), the residues were tempered at 773 K (6 days). For all solid solutions, the molar fractions of chromium and manganese, $x$(Cr) and $x$(Mn), respectively, were varied from 0 to 1. Figure 1 shows powders of $Mn(PO_3)_3$, $In_{0.4}Mn_{0.6}(PO_3)_3$, $(In_{0.2}Cr_{0.8})_4(P_2O_7)_3$, and $(In_{0.9}Cr_{0.1})_4(P_2O_7)_3$, to visualize the unexpected color changes.

Purple single crystals of $Mn(PO_3)_3$ with edge lengths of up to 0.4 mm were synthesized as a reference from manganese and dissolved in dilute nitric acid a 10-fold surplus of dilute phosphoric acid ($c$ = 1.00 mol/L). The reaction mixture was heated at 773 K for 3 weeks in a gold crucible. After this period, only the well-crystallized phosphate remained in the crucible, as the phosphoric acid had been slowly evaporated.

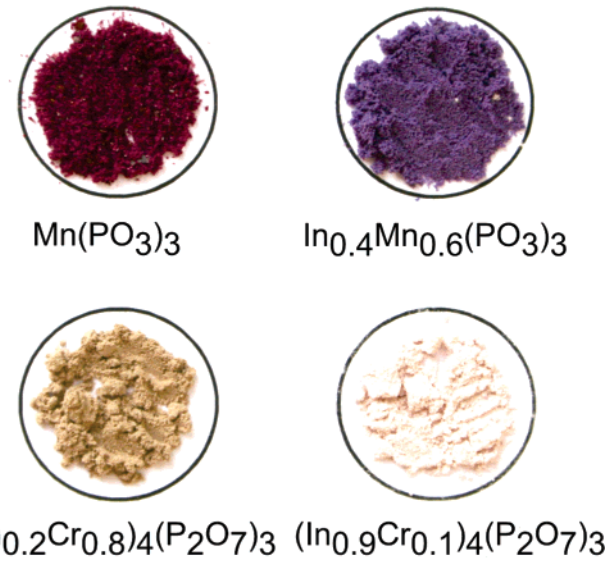


**Figure 1.** Powders of (a) $Mn(PO_3)_3$, (b) $In_{0.4}Mn_{0.6}(PO_3)_3$, (c) $(In_{0.2}Cr_{0.8})_4(P_2O_7)_3$, and (d) $(In_{0.9}Cr_{0.1})_4(P_2O_7)_3$, visualizing variations of color with changing dopant concentration.

**X-ray Diffraction.** Guinier images (Cu $K\alpha_1$, α-quartz as an internal standard) of all powders were recorded using a FR-352 camera (Enraf Nonius) with image-plate foil (BAS-MS 2325, Fuji Photo Film).[12,13] After exposure, the foil was scanned using the BASREADER system.[14] Lattice parameters (Figure 2) were refined from the powder data using the computer program SOS.[15]

**Spectroscopic Investigations.** Powder reflectance spectra of the single-phase solid solutions (Figure 3) were measured in the range of 5500−35000 $cm^{-1}$ using a Cary 2400 spectrophotometer (Varian) with $BaSO_4$ as the white standard. Single-crystal spectra of $Mn(PO_3)_3$ (Figure 4) were measured using a microcrystal UV/vis/NIR spectrophotometer.[16,17] Band positions (transition energies) were estimated visually from the observed UV/vis/NIR spectra. In three cases [$In_{0.8}Cr_{0.2}O_4$, $In_{0.5}Cr_{0.5}PO_4$, and $Cr_4(P_2O_7)_3$], Gauss curves were fit to the observed spectra.

**EDX analyses** (scanning tunnel microscope, DMS 940, Zeiss) were used to confirm the microscopic homogeneity of the samples. In addition, these analyses gave no indication for impurity elements.

## Results

The solid solution $In_{1-x}Cr_x(PO_3)_3$ covers the whole range $0 \le x \le 1$. Lattice parameters are given in Figure 2a. The strongest superstructure reflection, (0 2 0), indicating the presence of a tripled $b$-axis, was observed for all samples of the solid solution. An intensification of the green tint with increasing chromium content was observed. The electronic

(8) Palkina, K. K.; Maksimova, S. I.; Chibiskova, N. T.; Chudinova, N. N.; Karmanovskaya, N. B. *Neorg. Khim.* **1993**, *38*, 1270.
(9) Thauern, H.; Glaum, R. *Z. Anorg. Allg. Chem.* **2003**, *629*, 479.
(10) Mooney, R. C. L. *Acta Crystallogr.* **1956**, *9*, 113.
(11) Reinen, D. *Theor. Chim. Acta (Berlin)* **1966**, *5*, 301.
(12) Amemiya, Y.; Miyahara, J. *Nature* **1988**, *336*, 39.
(13) Bio-Imaging-Analyser IPR1800, Fuji Photo Film Co., Ltd., Tokyo, Japan.
(14) Version 2.2, Raytest Isotope Scanning Devices GmbH, Straubenhardt, Germany, 1999.
(15) Soose, J.; Meyer, G. *SOS: Program for Calculation of Unit Cell Parameters*; University of Giessen, Giessen, Germany, 1985.
(16) Krausz, E. *Aust. J. Chem.* **1993**, *46*, 1041.
(17) Krausz, E. *AOS News* **1998**, *12*, 21.

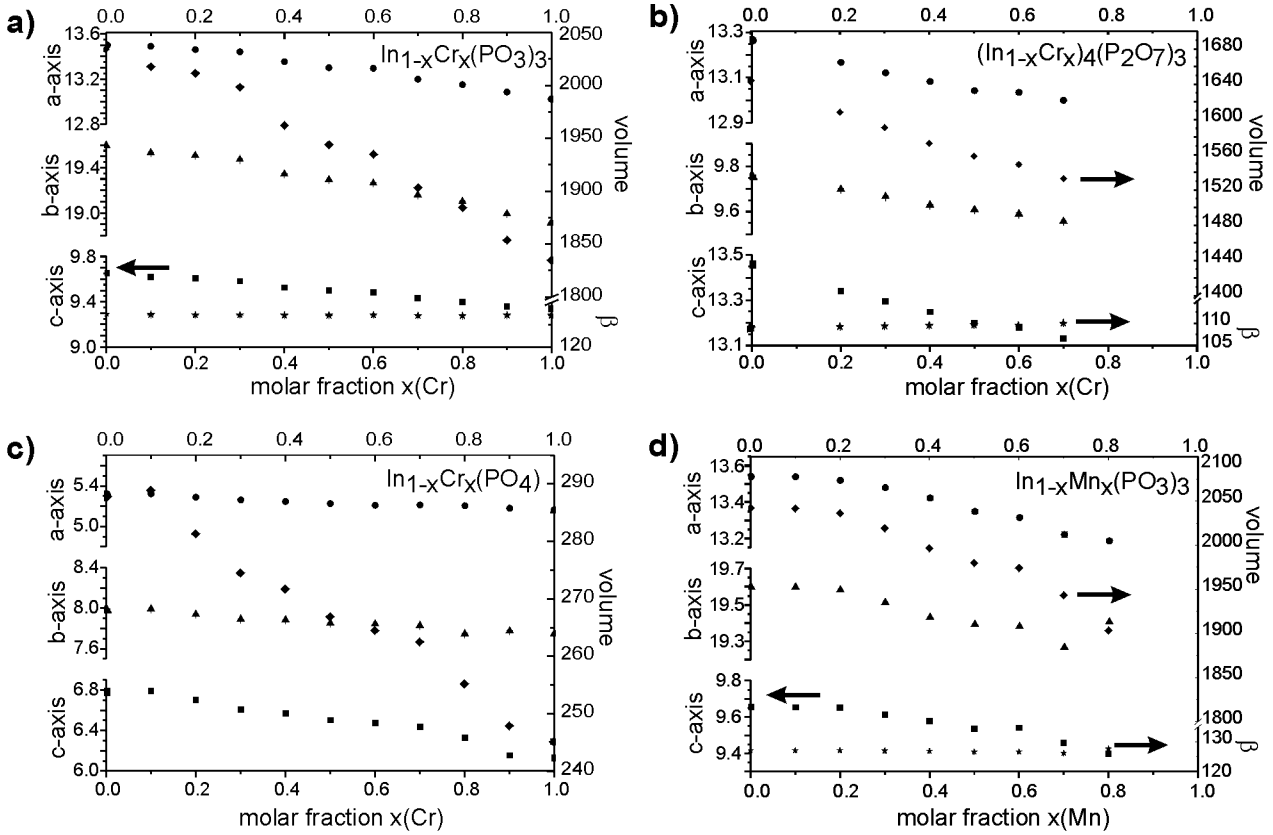


**Figure 2.** Vegard plots for the solid solutions (a) $In_{1-x}Cr_x(PO_3)_3$ ($0 \le x \le 1$), (b) $(In_{1-x}Cr_x)_4(P_2O_7)_3$ ($0 \le x \le 0.7$), (c) $In_{1-x}Cr_xPO_4$ ($0 \le x \le 1$), and (d) $In_{1-x}Mn_x(PO_3)_3$ ($0 \le x \le 0.8$). Lattice parameters (●) *a*, (▲) *b*, and (■) *c* in Å; (◆) *V* in Å$^3$; and (★) $\beta$ (deg) for monoclinic crystals. Arrows indicate the corresponding ordinate axis.

spectra (Figure 3a) show that this change was accompanied by a small blue shift (~900 cm$^{-1}$) of the spin-allowed electronic transitions $^4A_{2g} \rightarrow {}^4T_{2g}$ ($\tilde{\nu}_1$) and $^4A_{2g} \rightarrow {}^4T_{1g}(^4F)$ ($\tilde{\nu}_2$) and a larger shift of ~2000 cm$^{-1}$ for the $^4A_{2g} \rightarrow {}^4T_{1g}(^4P)$ ($\tilde{\nu}_3$) transition outside the visible region (Figure 3a and 5a). The dip in the absorption bands at $\tilde{\nu} \approx 14800$ cm$^{-1}$, denoted as $\tilde{\nu}(^2E)$, is caused by Fano antiresonance[18−20] between the $^2E_g$ state and the spin−orbit-split terms of the $^4T_{2g}$ state. The energy for the spin-forbidden transition $^4A_{2g} \rightarrow {}^2E_g$ remains constant for the whole solid solution within the measurement accuracy. Figure 3a shows representative spectra for $x = 0.2$, 0.5, 0.8, and 1.0. Observed transition energies as a function of $x$(Cr) are summarized in Figure 5a.

According to the Guinier images (Figure 2b), the homogeneity range for $(In_{1-x}Cr_x)_4(P_2O_7)_3$ is $0 \le x \le 0.7$. For higher amounts of $Cr_4(P_2O_7)_3$, a two-phase region containing $(In_{1-x}Cr_x)_4(P_2O_7)_3$ [$x = 0.7$, $In_4(P_2O_7)_3$ structure type[9]] and $Cr_4(P_2O_7)_3$ [$V_4(P_2O_7)_3$ structure type[21]] is observed. The color of the solid solution shifts from pink [$x$(Cr) = 0.1] to brownish [$x$(Cr) = 0.7]. Powders of pure $Cr_4(P_2O_7)_3$ are brownish-red. The energy of the first electronic transition $^4A_{2g} \rightarrow {}^4T_{2g}$, (term symbols given for $O_h$ symmetry) in the series $(In_{1-x}Cr_x)_4(P_2O_7)_3$ (Figure 3b) is 600−1800 cm$^{-1}$ lower in energy than observed for the metaphosphate series. With increasing $x$(Cr), a slight reduction (~280 cm$^{-1}$) of the energy of the spin-forbidden transition $^4A_{2g} \rightarrow {}^2E_g$ is observed, in contrast to the behavior of the other solid solutions containing chromium. A splitting of the $\tilde{\nu}_2$ transition, $^4A_{2g} \rightarrow {}^4T_{1g}(^4F)$, into two bands because of the lower symmetry (approximately $C_{3v}$) of the $[Cr^{III}O_6]$ chromophore in $(In_{1-x}Cr_x)_4(P_2O_7)_3$ is supported by Gauss fitting. The energy difference between these two bands ($\tilde{\nu}_{2a}$ and $\tilde{\nu}_{2b}$ in Figures 3b and 5b) grows slightly with $x$(Cr). The blue shift (~1200 cm$^{-1}$) of the third transition $^4A_{2g} \rightarrow {}^4T_{2g}(^4P)$ is smaller than in $In_{1-x}Cr_x(PO_3)_3$. Representative spectra of $(In_{1-x}Cr_x)_4(P_2O_7)_3$ ($x = 0.2$, 0.5, and 1.0) are given in Figure 3b. Figure 5b summarizes the dependence of the transition energies on $x$(Cr).

For the isotypic orthophosphates $InPO_4$[10] and $\beta$-$CrPO_4$,[22] complete miscibility according to $In_{1-x}Cr_xPO_4$ ($0 \le x \le 1$) is observed. The lattice parameters (Figure 2c) show that substitution of indium(III) by the smaller chromium(III) ions leads to a pronounced shrinking of the *c*-axis, whereas the effect on the *a*- and *b*-axes is much less developed. [Note that the lattice parameters determined for pure $InPO_4$, $a$ = 5.316(1) Å, $b$ = 7.983(1) Å, $c$ = 6.781(1) Å, differ significantly from those given in ref 10.) A shift in color from pink to grayish-green is observed for $In_{1-x}Cr_xPO_4$. In this series (Figure 3c), the first electronic transition $^4A_{2g} \rightarrow$

(18) Voda, M.; Garcia Sole, J.; Jaque, F.; Vergara, I.; Kaminskii, A.; Mill, B.; Butashin, A. *Phys. Rev. B* **1994**, *49*, 3755.
(19) Fano, U. *Phys. Rev.* **1961**, *124*, 1866.
(20) Neuhauser, D.; Park, T. J.; Zink, J. I. *Phys. Rev. Lett.* **2000**, *85*, 5304.
(21) Palkina, K. K.; Maksimova, S. I.; Chibiskova, N. T.; Schlesinger, K.; Ladwig, G. *Z. Anorg. Allg. Chem.* **1985**, *529*, 89.
(22) Attfield, J. P.; Battle, P. D.; Cheetham, A. K. *J. Solid State Chem.* **1985**, *57*, 357.

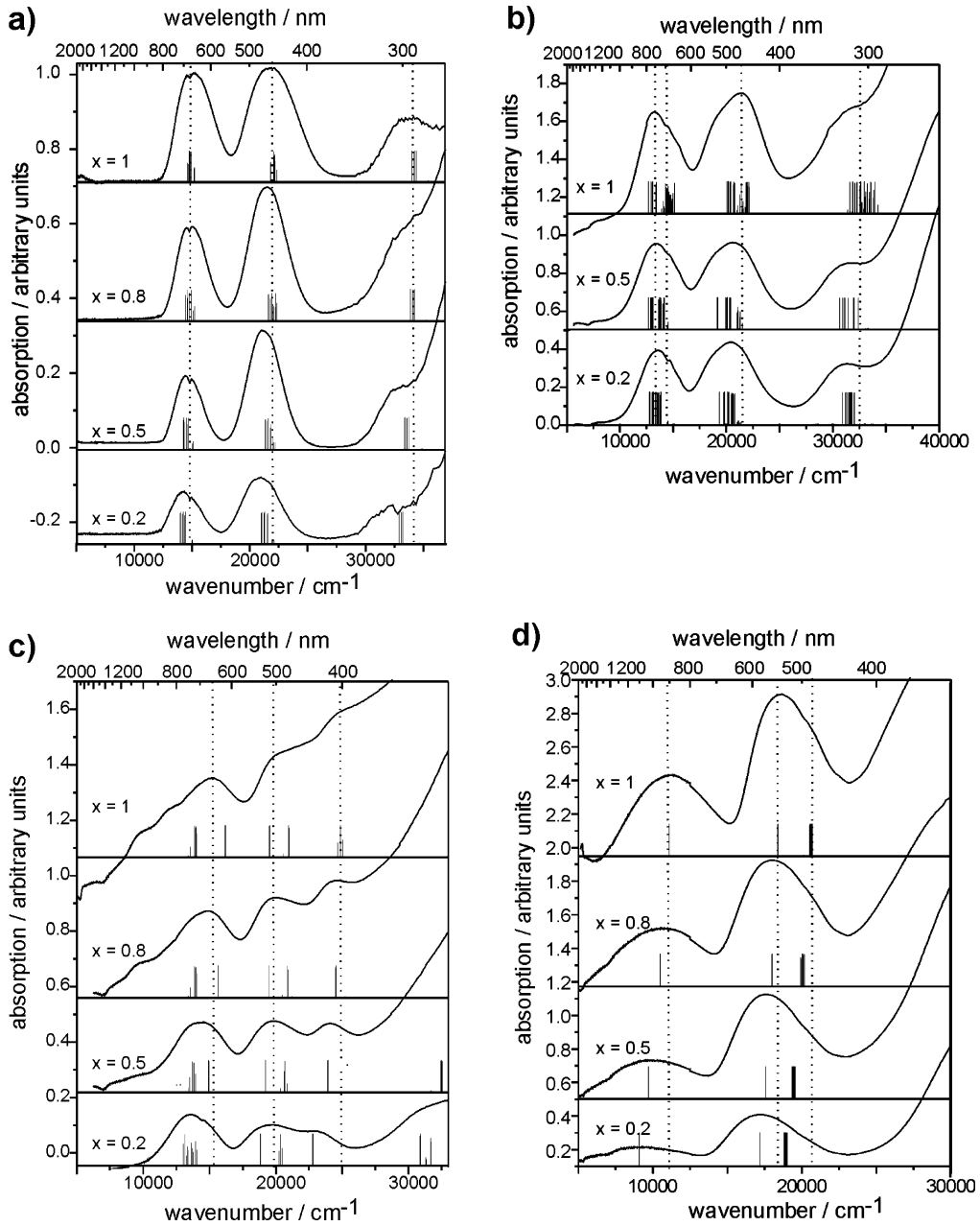


**Figure 3.** Representative powder reflectance spectra and d−d-transition energies from AO modeling of (a) $In_{1-x}Cr_x(PO_3)_3$, (b) $(In_{1-x}Cr_x)_4(P_2O_7)_3$, (c) $In_{1-x}Cr_xPO_4$, and (d) $In_{1-x}Mn_x(PO_3)_3$. Dotted lines are meant as a guide to the eye, to visualize the variation in the spectra upon doping.

$^4T_{2g}$ shifts considerably by about 1700 $cm^{-1}$ to the blue with increasing $x$(Cr). The second transition, $^4A_{2g} \rightarrow {}^4T_{1g}(^4F)$, is clearly split into two bands ($\tilde{\nu}_{2a}$ and $\tilde{\nu}_{2b}$) because of the low symmetry of the chromophore. Similarly to the diphosphate series, a slight increase of the energy difference between the two split states is observed with increasing $x$(Cr). The third transition, $^4A_{2g} \rightarrow {}^4T_{1g}(^4P)$, is obscured by low-lying charge-transfer transitions. The development of transition energies with $x$(Cr) is shown in Figure 5c. In contrast to the other mixed indium/chromium phosphates, the spectra of the series $In_{1-x}Cr_xPO_4$ (Figure 3c) show additional absorption bands in the NIR region (9000−12500 $cm^{-1}$) with increasing $x$(Cr). These bands clearly cannot be related to any kind of d−d transition of an octahedral $[Cr^{III}O_6]$ chromophore.

Indium(III) metaphosphate[8] and manganese(III) metaphosphate[23] show a miscibility gap for higher amounts of Mn-$(PO_3)_3$ ($x > 0.8$). For $In_{1-x}Mn_x(PO_3)_3$ ($0 \le x \le 0.8$) (Figure 2d), the solid solution adopts the structure of pure $In(PO_3)_3$ [8]. The mixed crystal series shows variation of its color from light blue to purple. This change is reflected in the spectra (Figures 3d and 5d) by a blue shift of the two absorption bands $^5B_{1g} \rightarrow {}^5A_{1g}$ (∼2100 $cm^{-1}$) and $^5B_{1g} \rightarrow {}^5B_{2g}$, $^5E_g$ (∼1000 $cm^{-1}$) with increasing $x$(Mn) [band assignment according to $D_{4h}$, elongated (see subsection b, Chromophore Geometries, below). Thereby, the energy difference between these two transitions is reduced (Figure 5d).

(23) Bagieu-Beucher, M. *Acta Crystallogr.* **1978**, *B34*, 1443.

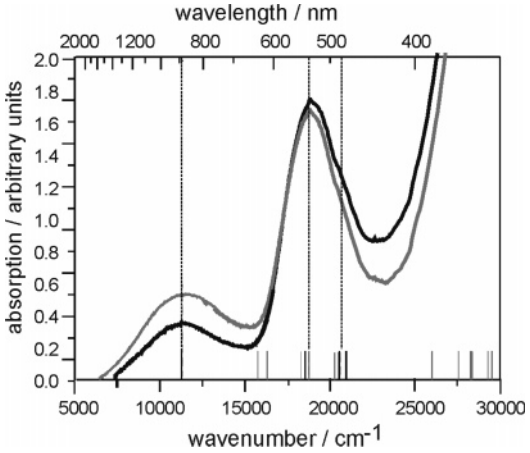


**Figure 4.** Single-crystal spectra of $Mn(PO_3)_3$ (gray, horizontal polarization; black, vertical polarization on an arbitrary crystal face) with the calculated d−d-transitions [$\tilde{\nu}_1$, $^5B_{1g}(^5E_g) \rightarrow {}^5A_{1g}(^5E_g)$; $\tilde{\nu}_2$, $^5B_{1g}(^5E_g) \rightarrow {}^5B_{2g}$, $^5E_g(^5T_{2g})$]. Black, spin-allowed transition; gray, spin-forbidden transition. Dotted lines are meant as a guide to the eye for a better comparison of observed spectra and calculated transition energies.

The shifts $\delta(\tilde{\nu}_i)$ for each absorption band going from the lowest [$x$(Cr/Mn) = 0.1] to the highest [$x$(Cr/Mn) = 1] dopant concentration are summarized in Table 1.

**Angular Overlap Modeling. (a) Parameters.** For a better understanding of the correlation between radial and angular distortion of the chromophores and their d-electron energies, calculations within the framework of the angular overlap model (AOM)[24−26] were performed. An advantage of this model is its ability to use the chromophores with their actual geometries, known from crystal structure analysis. Instead of using global parameters, such as 10$Dq$ or $\Delta$, one $\sigma$- and two $\pi$-interactions (a 18 total bonding parameters for an octahedral complex) of each ligand with the five 3d orbitals of the central ion are used for the fitting between calculated and observed transition energies. The decomposition of the global ligand-field parameter (10$Dq$ or $\Delta$) allows, in particular, for symmetry effects due to the second-sphere ligand field, e.g., the competition between the central ion and neighboring cations for the p-electrons of bridging oxygen atoms, to be taken into account. To reduce the number of independent bonding parameters, relations between some of the parameters were introduced. Thus, for the energy $e_\sigma$(M−O), proportionality to the distance $d$(M−O)$^{-5.0}$ was assumed [5]. The energy $e_\pi$ was set to one-quarter of the corresponding energy $e_\sigma$ in the case of an "undisturbed" $\pi$-interaction,[26] as depicted in Figure 6b. Thus, for oxygen atoms with a coordination number (CN) of 2, $e_{\pi,x}$ and $e_{\pi,y}$ are equal. In the simplest case, these relations reduce the 18 interaction energies to only one independent parameter, which is recommended to be $e_{\sigma,\max}$(M−O) for the shortest $d$(M−O).

In the modeling of the d electronic levels of $Cr^{3+}$ in the mixed chromium(III)/indium(III) phosphates, anisotropic $\pi$-interactions between $Cr^{3+}$ and oxygen were taken into account. Anisotropic $\pi$-interactions were assumed for oxygen atoms with two or more metal atoms as bonding partners, resulting in different values for $e_{\pi,x}$ and $e_{\pi,y}$. The $\pi$-interactions perpendicular to the plane formed by $P^V$ and $M^{III}$ coordination (see, for example, Figure 6b,c) are described by $e_{\pi,y}$, whereas $e_{\pi,x}$ is the in-plane $\pi$-interaction (Figure 6). The $\pi$-interaction energy, $e_{\pi,x}$, can be equal to or less than $e_{\pi,y}$ depending on the number of cationic neighbors and the angles involved. This anisotropy might be caused by competition of the $\sigma$-interaction between $d_{z^2-x^2}$ on M2 and $p_z$ on the bridging oxygen and of the $\pi$-interaction between $d_{zx}$ on M1 and the same p-orbital (Figure 6a). Alternatively, the differences between $e_{\pi,x}$ and $e_{\pi,y}$ can be approximately visualized in a simple hybridization model. In the case of CN($O^{2-}$) = 2 (M + P), the linear $sp_z$ hybridization on oxygen allows two $\pi$-interactions perpendicular to $z$ (Figure 6b). For CN($O^{2-}$) = 3 (2M + P), $sp^2$ hybridization on oxygen reduces the $\pi$-interaction to an interaction via $p_y$ (Figure 6c). Finally, $sp^3$ hybridization for CN($O^{2-}$) = 4 (3M + P) leaves no oxygen orbitals for a $\pi$-interaction with the metal (Figure 6d), at least in such a coarse bonding scheme. Thus, the $\pi$-bonding abilities of oxygen with coordination numbers 2, 3, and 4 are similar to those of $F^-$, $H_2O$, and $NH_3$,[26] respectively.

During modeling of the particular bonding situation of $Mn^{3+}$ in the solid solution $In_{1-x}Mn_x(PO_3)_3$, $d_{z^2}$−s mixing[27,28] in the Jahn−Teller-induced $D_{4h}$ geometry and variations in the radial distortion of the [$Mn^{III}O_6$] chromophore were taken into account.

Interelectronic repulsion is introduced into the AOM calculations via the Racah parameters $B$ and $C$ ($cm^{-1}$), and spin−orbit coupling is introduced by $\xi$ ($cm^{-1}$). For AO modeling, the free ion ratios $C_0/B_0 = 4.0$ for $Cr^{3+}$ and $C_0/B_0 = 4.3$ for $Mn^{3+}$ were used and retained during the calculations.[26] Variations in the covalency of the M−O interaction in the complexes were considered by variable nephelauxetic ratios $\beta$ [$\beta = B/B_0$; $B_0(Cr^{3+}) = 933$ $cm^{-1}$, $B_0(Mn^{3+}) = 950$ $cm^{-1}$].[26] The spin−orbit coupling parameter $\xi$ was also assumed to be reduced relative to the free ion values [$\xi_0(Cr^{3+}) = 275$ $cm^{-1}$, ($\xi_0(Mn^{3+}) = 355$ $cm^{-1}$] according to $\beta$.

For the calculations, the PC program CAMMAG,[29,30] in a modified version,[31] was used. Best-fit AOM parameters for the various spectra are summarized in Table 2.

**(b) Chromophore Geometries.** The AOM calculations for the solid solutions were based on the chromophore geometries derived from the crystal structures of $Cr(PO_3)_3$,[32] $In_4(P_2O_7)_3$,[9] $\beta$-$CrPO_4$[22] and $Mn(PO_3)_3$.[23] To date, no structure refinement is available for $Cr_4(P_2O_7)_3$.

In $Cr(PO_3)_3$ three crystallographically independent, isolated [$Cr^{III}O_6$] octahedra (Figure 7a) are found. The angular distortion for each of these units is less than 7° with respect

(24) Jørgensen, C. K.; Pappalardo, R.; Schmidtke, H. H. *J. Chem. Phys.* **1963**, *39*, 1422.
(25) Richardson, D. E. *J. Chem. Educ.* **1993**, *70*, 372.
(26) Figgis, B. N.; Hitchman, M. A. *Ligand Field Theory and Its Applications*; Wiley-VCH, New York, 2000.
(27) Ford, R. J.; Hitchman, M. A. *Inorg. Chim. Acta* **1979**, *33*, L167.
(28) Smith, D. W. *Inorg. Chim. Acta* **1977**, *22*, 107.
(29) Cruse, D. A.; Davies, J. E.; Harding, J. H.; Gerloch, M.; Mackey, D. J.; McMeeking, R. F. *CAMMAG, a FORTRAN program*; Cambridge, 1980.
(30) Gerloch, M. *Magnetism and Ligand Field Theory*; Cambridge University Press: Cambridge, U.K., 1983.
(31) Riley, M. *CAMMAG for PC*, version 4.0; University of Queensland: St. Lucia, Australia, 1997.
(32) Gruss, M.; Glaum, R. *Acta Crystallogr.* **1996**, *C52*, 2647.

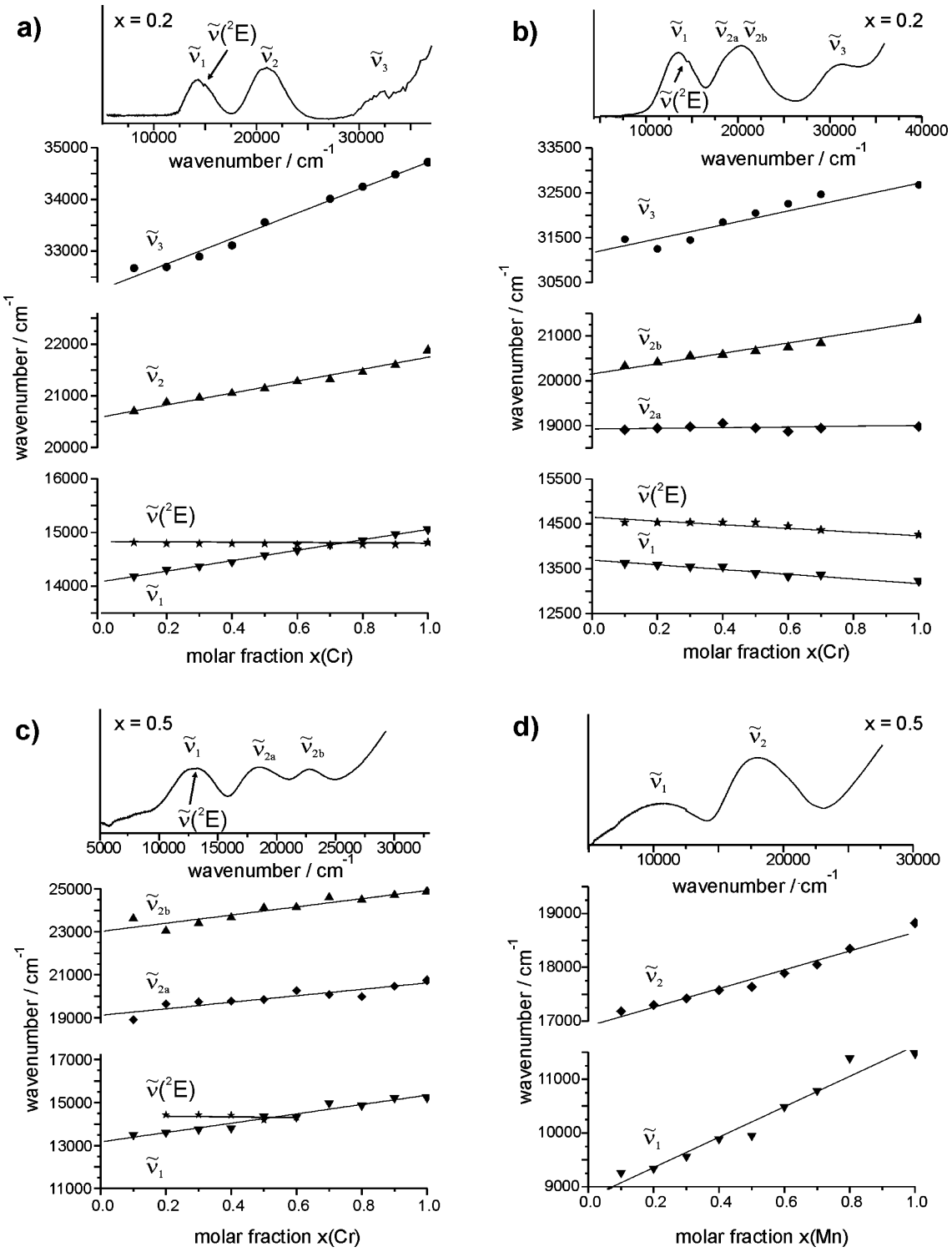


**Figure 5.** Energies of the d−d electronic transitions of the solid solutions (a) $In_{1-x}Cr_x(PO_3)_3$, (b) $(In_{1-x}Cr_x)_4(P_2O_7)_3$, (c) $In_{1-x}Cr_xPO_4$, and (d) $In_{1-x}Mn_x(PO_3)_3$ as a function of $x$(Cr/Mn). For better clarity, representative spectra of the solid solutions are included. $\tilde{\nu}_1$, $\tilde{\nu}_2$, and $\tilde{\nu}_3$ are the octahedral $^4A_{2g} \rightarrow {}^4T_{2g}$, $^4T_{1g}(^4F)$, and $^4T_{1g}(^4P)$ bands of the $[Cr^{III}O_6]$ chromophore, and $\tilde{\nu}(^2E)$ refers to the spin-forbidden $^4A_{2g} \rightarrow {}^2E_g(^2G)$ transition (a−c). For the definition of $\tilde{\nu}_1$ and $\tilde{\nu}_2$ in the case of $Mn^{III}$ and for further details, see the text.

to the ideal octahedron. The radial distortion, $\Delta d$(Cr−O) (difference between the longest and the shortest Cr−O distances), increases in the series $\Delta d$(Cr2−O) = 0.013 Å, $\Delta d$(Cr1−O) = 0.022 Å, $\Delta d$(Cr3−O) = 0.053 Å, but is still rather small. All oxygen ligands have a coordination number of 2 (one $M^{3+}$ and one $P^{5+}$). No oxygen ligand is shared between adjacent $M^{3+}$ ions.

In $In_4(P_2O_7)_3$, two crystallographically different $[In^{III}O_6]$ octahedra share a common face, thus forming $[In_2O_9]$ units (Figure 7b).[9] The bridging oxygen atoms are coordinated by two indium and one phosphorus atom. The terminal oxygen atoms have coordination number 2 (In + P). Indium−oxygen distances, $d$(In−O), are about 2.20 Å for the bridging atoms and markedly shorter for the terminal atoms, $d$(In−O) ≈ 2.08

**Table 1.** Shifts in the Energy of the d−d Electronic Transitions between the Sample with the Highest Amount of Transition Metal ($x$ = 1) and the Lowest Dopant Concentration $x$(Cr/Mn) = 0.1[a]

| | transition | | | |
|---|---|---|---|---|
| compound | $\delta(\tilde{\nu}_1)$[b] | $\delta[\tilde{\nu}(^2E)]$[b] | $\delta(\tilde{\nu}_{2a})$, $\delta(\tilde{\nu}_{2b})$[b] | $\delta(\tilde{\nu}_3)$[b] |
| $In_{1-x}Cr_x(PO_3)_3$ | 875 | 0 | 1175[c] | 2050 |
| $(In_{1-x}Cr_x)_4(P_2O_7)_3$ | −340 | −280 | 70, 1040 | 1210 |
| $In_{1-x}Cr_xPO_4$ | 1740 | 0 | 1200, 2000 | − |

| | $\delta(\tilde{\nu}_1)$[b] | $\delta(\tilde{\nu}_2)$[b] |
|---|---|---|
| $In_{1-x}Mn_x(PO_3)_3$ | 2220 | 1640 |

[a] $\delta(\tilde{\nu}_1)$ mirrors the change of the octahedral ligand-field strength Δ in the case of $Cr^{3+}$ ($\equiv {}^4A_{2g} \rightarrow {}^4T_{2g}$). [a] $\delta(\tilde{\nu}) = \tilde{\nu}(x = 1) - \tilde{\nu}(x = 0.1)$. [b] Transitions $\tilde{\nu}_{2a}$ and $\tilde{\nu}_{2b}$ are not resolved.

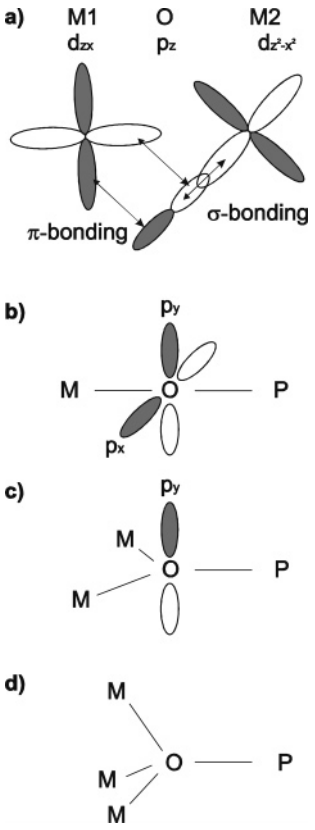


**Figure 6.** Schematic visualization of anisotropic $\pi$ bonding between an oxygen ligand and a metal center. (a) Competition between $d_{zx}$ and $d_{z^2-x^2}$ orbitals of adjacent metal ions for $\sigma$ or $\pi$ overlap with a $p_z$ orbital of a bridging oxygen. (b) $e_{\pi,x} = e_{\pi,y}$ for approximately linear coordinated oxygen. (c) $e_{\pi,x} < e_{\pi,y}$ for oxygen having three bonding partners. (d) $e_{\pi,x} = e_{\pi,y} \approx 0$ for $sp^3$-hybridized oxygen having four bonding partners.

Å. To a first approximation, the $[In^{III}O_6]$ octahedra belong to the point group $C_{3v}$, although the true symmetry is $C_1$.

There is only one type of $[Cr^{III}O_6]$ unit in $\beta$-$CrPO_4$, and it exhibits a compressed octahedral geometry with four equatorial oxygen atoms at a distance of 2.03 Å (Figure 7c) and an axial bond distance of $d(Cr-O_{ax}) = 1.93$ Å [22]. By sharing of two opposite edges, the octahedra form infinite chains. The bridging oxygen atoms show three-fold coordination (2Cr + P), whereas the axial oxygen atoms are only two-fold-coordinated (Cr + P).

One isolated $[Mn^{III}O_6]$ octahedron is observed in $Mn(PO_3)_3$ (Figure 7d).[23] It is elongated with the equatorial oxygen atoms at distances of $d(Mn-O_{eq}) = 1.88$ and 1.91 Å and an axial bond distance of $d(Mn-O_{ax}) = 2.16$ Å. All oxygen atoms have coordination number 2 (Mn + P).

**(c) AOM Fitting Procedure.** Calculations were carried out for the lowest, the highest, and several intermediate dopant concentrations. In all cases, the transition energies of the pure transition-metal phosphates were modeled first. In subsequent calculations, the band shifts observed for the solid solutions were matched by variation of the AOM parameters $e_{\sigma,max}$, $B$, and the ratio $e_{\pi,x}/e_{\pi,y}$ for bridging oxygen atoms. All crystallographically independent metal sites were taken into account in the modeling procedure for $In_{1-x}Cr_x(PO_3)_3$ and $(In_{1-x}Cr_x)_4(P_2O_7)_3$.

For the calculations for $In_{1-x}Cr_x(PO_3)_3$, the values $e_\sigma(M-O) \approx d(M-O)^{-5}$ and $e_{\pi,x} = e_{\pi,y} = {}^1/_4 e_\sigma$ (isotropic $e_\pi$) were assumed. The best match (Figure 3a) of the observed transition energies for pure $Cr(PO_3)_3$ was obtained using $e_{\sigma,max}(Cr-O) = 8300$ cm$^{-1}$ for the shortest distance $d(Cr-O) = 1.927$ Å and $\beta = 0.84$. The spectra of solid solutions $In_{1-x}Cr_x(PO_3)_3$ with lower chromium concentrations (Figure 3a) could be fitted by reducing $e_{\sigma,max}$ to 7900 cm$^{-1}$ and keeping $B/B_0 = 0.84$. Figure 3a compares calculated and observed transition energies for $x = 0.2$, 0.5, 0.8, and 1.0.

AOM calculations for $Cr_4(P_2O_7)_3$ using the distorted coordination geometry of $In_4(P_2O_7)_3$ (symmetry close to $C_{3v}$) and isotropic $\pi$-interactions between oxygen and $Cr^{3+}$ did not reproduce the observed spectra. In particular, the splitting of the absorption band $\tilde{\nu}_2$ (from a Gauss fit) was not matched. Introducing strongly anisotropic $\pi$-overlap ($e_{\pi,x} = 0.05 e_{\pi,y}$) for the bridging oxygen atoms allowed for the proper description of the split transition $\tilde{\nu}_2$. The observed transition energies were well reproduced with $e_{\sigma,max} = 8400$ cm$^{-1}$ and $\beta = 0.80$. The slight increase of this energy observed with rising indium content in the series $(In_{1-x}Cr_x)_4(P_2O_7)_3$ for $\tilde{\nu}_1$ (~400 cm$^{-1}$) and the spin-forbidden transition ${}^4A_{2g} \rightarrow {}^2E_g$ (~280 cm$^{-1}$) can be matched by small increases of $\beta$ (from 0.80 to 0.81) and $e_{\sigma,max}$ (from 8400 to 8700 cm$^{-1}$) in the AOM calculations. The reduction of the splitting of $\tilde{\nu}_2$ and the decreasing energies of $\tilde{\nu}_2$ and $\tilde{\nu}_3$ for smaller dopant concentrations can be reproduced in the AOM calculations by increasing $e_{\pi,x}$ from $0.05 e_{\pi,y}$ to $0.8 e_{\pi,y}$. Representative spectra and the results of their modeling are shown in Figure 3b for $x = 0.2$, 0.5, and 1.0.

The spectrum of $In_{0.8}Cr_{0.2}PO_4$ shows a clearly resolved splitting of the spin-allowed band $\tilde{\nu}_2$. From the Gauss fit, three components could be identified, in accordance with point group $D_{2h}$ of the chromophore. With $e_{\sigma,max} = 8000$ cm$^{-1}$ for the shortest distance $d(Cr-O) = 1.93$ Å and $\beta = 0.76$, the energy of the transitions could be fairly well described. However, for a more accurate fit, especially of the split terms of $\tilde{\nu}_2$, anisotropic $\pi$-interactions for the four bridging oxygen atoms according to $e_{\pi,x} = 0.8 e_{\pi,y}$ had to be introduced. At higher chromium concentrations, the energy difference between the split terms of $\tilde{\nu}_{2a}$ increased. This behavior could be reproduced in the calculations by using higher $\pi$-anisotropies [$e_{\pi,x}$ = (0.8 to 0.3) $e_{\pi,y}$ for pure $\beta$-$CrPO_4$].

In addition to the larger $\pi$ anisotropies, only small increases of $e_{\sigma,max}$ (from 8000 to 8200 cm$^{-1}$) were required

**Table 2.** Summary of Ligand-Field Splittings Δ and Best-Fit Parameters Obtained from the Modeling of the Transition Energies within the AOM Framework

| compound | chromophore[a] | $\Delta^b$ ($cm^{-1}$) | $e_{\sigma,max}{}^c$ ($cm^{-1}$) | $e_{\pi,x}/e_{\pi,y}{}^d$ | $\beta^e$ | $e_{ds}$ ($cm^{-1}$) |
|---|---|---|---|---|---|---|
| $Cr(PO_3)_3$ | 6 terminal at 1.93 ≤ | 15060 | 8300 | 1 | 0.84 | – |
| $In_{0.2}Cr_{0.8}(PO_3)_3$ | $d$(M−O) ≤ 1.98 Å | 14860 | 8200 | 1 | 0.84 | – |
| $In_{0.5}Cr_{0.5}(PO_3)_3$ | | 14580 | 8050 | 1 | 0.84 | – |
| $In_{0.8}Cr_{0.2}(PO_3)_3$ | | 14300 | 7900 | 1 | 0.84 | – |
| $Cr_4(P_2O_7)_3$ | 3 bridging at 2.02 ≤ | 13230 | 8400 | 0.05 | 0.80 | – |
| $(In_{0.5}Cr_{0.5})_4(P_2O_7)_3$ | $d$(M−O) ≤ 2.10 Å | 13400 | 8600 | 0.5 | 0.81 | – |
| $(In_{0.8}Cr_{0.2})_4(P_2O_7)_3$ | 3 terminal at 2.18 ≤ $d$(M−O) ≤ 2.30 Å | 13590 | 8700 | 0.8 | 0.81 | |
| $CrPO_4$[f] | 4 bridging at 2.03 Å, | 15060 | 8200 | 0.3 | 0.76 | |
| $In_{0.2}Cr_{0.8}PO_4$ | 2 terminal at 1.93 Å | 14860 | 8200 | 0.4 | 0.76 | |
| $In_{0.5}Cr_{0.5}PO_4$ | | 14580 | 8100 | 0.5 | 0.76 | |
| $In_{0.8}Cr_{0.2}PO_4$ | | 14300 | 8000 | 0.75 | 0.76 | |
| $Mn(PO_3)_3$[g] | 6 terminal at 1.88, 1.91, and 2.16 Å | 13080 | 9600 | 1 | 0.81 | 576 |
| $Mn(PO_3)_3$[h] | calculated with 4 short | 13080 | 9200, 4800 | 1 | 0.81 | 576 |
| $In_{0.2}Mn_{0.8}(PO_3)_3$[h] | and 2 long distances | 12650 | 9000, 4900 | 1 | 0.81 | 576 |
| $In_{0.5}Mn_{0.5}(PO_3)_3$[h] | | 12660 | 8800, 5100 | 1 | 0.81 | 576 |
| $In_{0.8}Mn_{0.2}(PO_3)_3$[h] | | 12630 | 8600, 5200 | 1 | 0.81 | 576 |

[a] Bonding status of oxygen and $d$(M−O) distances. [b] Δ evaluated from the average energy of the $\tilde{\nu}_1$ transition for $Cr^{3+}$ and from the difference ($\tilde{\nu}_2 - {}^1/_2\tilde{\nu}_1$) for $Mn^{3+}$. [c] Energy for the M−O $\sigma$-interaction corresponding to the shortest $d$(M−O) distance. [d] $e_{\pi,x}/e_{\pi,y}$ ratio for metal−metal bridging oxygen atoms; $e_{\pi,y} = {}^1/_4 e_\sigma$. [e] $B_0(Cr^{3+}) = 933$ $cm^{-1}$, $B_0(Mn^{3+}) = 950$ $cm^{-1}$, and the free ion ratios $C_0/B_0 = 4.0$ for $Cr^{3+}$ and $C_0/B_0 = 4.3$ for $Mn^{3+}$ were used in the calculations.[26] The spin−orbit coupling parameter $\xi$ was reduced relative to the free ion values [$\xi_0(Cr^{3+}) = 275$ $cm^{-1}$, $\xi_0(Mn^{3+}) = 355$ $cm^{-1}$] according to $\beta$. [f] $\beta$ modification.[22] [g] Three different $e_\sigma$ values corresponding to three $d$(Mn−O) distances were used for modeling of the [$Mn^{III}O_6$] chromophore in pure $Mn(PO_3)_3$. [h] For a simplified AOM treatment, the [$Mn^{III}O_6$] chromophore in the solid solutions was modeled using only two different values for $e_\sigma$, corresponding to the four equatorial and the two axial oxygen atoms.

to reproduce the observed shift of the spectra to higher energies for increasing $x$(Cr). Figure 3c shows calculated and observed transitions for $x = 0.2$, 0.5, 0.8, and 1.0.

The modeling for the series $In_{1-x}Mn_x(PO_3)_3$ started from the single-crystal spectrum of $Mn(PO_3)_3$ (Figure 4). Without allowing for d−s mixing, only the energy of the split bands of the second transition $\tilde{\nu}_2$ (Figures 3d, 4, and 5d) could be fitted satisfactorily [$e_{\sigma,max} = 9600$ $cm^{-1}$ for $d$(Mn−O) = 1.88 Å, Racah parameter $B = 81\%$ of the free ion value]. To reproduce the energy difference between the two transitions at $\tilde{\nu}_1$ and $\tilde{\nu}_2$, the introduction of d−s mixing, parametrized by the energy $e_{ds}$, was necessary. With $e_{ds} = 576$ $cm^{-1}$, the calculated and observed transition energies were in good agreement. Again, for all fits, $e_{\pi,x} = e_{\pi,y} = {}^1/_4 e_\sigma$ was assumed.

As Figure 5d shows, the energies of the absorption bands $\tilde{\nu}_1$ and $\tilde{\nu}_2$ of the solid solution $In_{1-x}Mn_x(PO_3)_3$ decrease with decreasing manganese content, but $\tilde{\nu}_1$ is affected to a much greater extent. These shifts could be matched in the AO modeling with a reduction of $e_{\sigma,eq}$ (for the four equatorial oxygen atoms) from 9200 $cm^{-1}$ [pure $Mn_x(PO_3)_3$] to 8600 $cm^{-1}$ [$In_{0.8}Mn_{0.2}(PO_3)_3$] and a simultaneous increase of $e_{\sigma,ax}$ from 4800 to 5200 $cm^{-1}$. Changing $e_{ds}$ from 576 to 270 $cm^{-1}$ while reducing $e_{\sigma,max}$ from 9600 to 9000 $cm^{-1}$ and retaining the ratio between the $e_\sigma$ energies also allowed a fit to the observed spectra.

Results of the fittings compared to the experimental results for $x$(Mn) = 0.2, 0.5, and 1.0 are shown in Figure 3d. Table 2 summarizes the results of the AOM calculations.

## Discussion

Complete miscibility with nice Vegard behavior of the lattice parameters is observed for mixed indium/chromium meta- and orthophosphates. For the series $(In_{1-x}Cr_x)PO_4$, substitution of $In^{3+}$ by the smaller $Cr^{3+}$ leads to a pronounced shrinking of the crystallographic $c$-axis of the orthorhombic unit cell, which is 5 times larger than that of the $a$- and $b$-axes (Figure 2c). This behavior can be rationalized from the structure (Figure 7c), assuming that the chains of [$M^{III}O_6$] octahedra are much more susceptible to shrinking than the distances between the chains. Solid solutions $(In_{1-x}Cr_x)_4(P_2O_7)_3$ are possible for $0 \le x \le 0.7$. In contrast, the solubility of $In_4(P_2O_7)_3$ in $Cr_4(P_2O_7)_3$ with the $V_4(P_2O_7)_3$[21] structure is negligible, which is an unexpected observation, given the close similarity of the two structures.

Up to 80 mol % $Mn(PO_3)_3$ can be substituted isomorphously into $In(PO_3)_3$, giving $In_{1-x}Mn_x(PO_3)_3$ ($0 \le x \le 0.8$). For $0.80 \le x(Mn) \le 1.00$, a two-phase region consisting of $In_{0.2}Mn_{0.8}(PO_3)_3$ and $Mn(PO_3)_3$ exists. The X-ray powder diffraction pattern gives no hint of a significant solubility of $In(PO_3)_3$ in the manganese(III) metaphosphate host lattice. Comparison of Figure 2a with 2d shows that substitution of $In^{3+}$ by $Cr^{3+}$ and $Mn^{3+}$ gives very similar changes of the lattice parameters determined for $In_{1-x}Cr_x(PO_3)_3$ and $In_{1-x}Mn_x(PO_3)_3$.

Within the framework of the angular overlap model, descriptions of the spectra of the solid solutions and of pure chromium/manganese phosphates are possible by using self-consistent sets of AOM parameters for the chromophores [$Cr^{III}O_6$] and [$Mn^{III}O_6$]. The magnitude of the excited-state splitting can be correlated with the geometric distortion of the [$MO_6$] polyhedra. It also depends on variations of the d−p $\pi$-interactions between $Cr^{3+}$ and $O^{2-}$.

There appears to be a tendency to lower interelectronic repulsion parameters for $Cr^{3+}$ in the sequence metaphosphate, diphosphate, monophosphate (Table 2). Whether this is only partly a significant effect is open to question, because the transition at $\tilde{\nu}_2$, from which $B$ is evaluated, depends only weakly on $B$. In contrast to the series $In_{1-x}Cr_x(PO_3)_3$ and

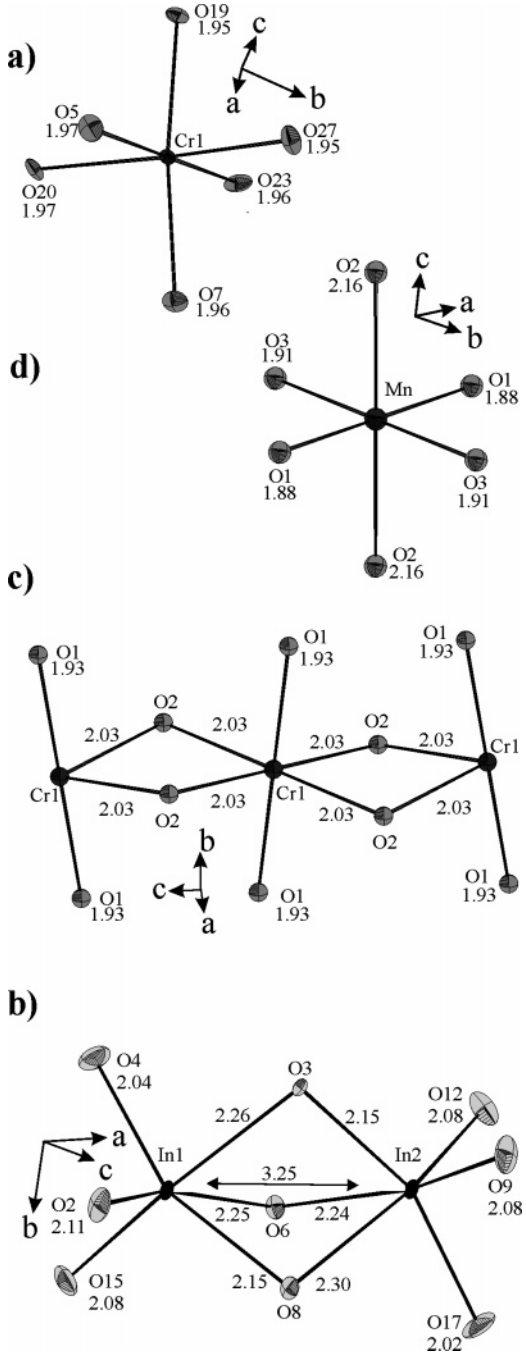


**Figure 7.** ORTEP plot of the following chromophores (ATOMS, version 6.2[38]): (a) $CrO_6$ octahedra in $Cr(PO_3)_3$, (b) $In_2O_9$ octahedra pairs in $In_4(P_2O_7)_3$, (c) part of the octahedral chains in $InPO_4$, (d) $MnO_6$ octahedra in $Mn(PO_3)_3$. Pale gray, $O^{2-}$; dark gray, In and Mn. In addition to the metal ions, every oxygen has one cationic $P^V$ neighbor.

$(In_{1-x}Cr_x)PO_4$, in which $\tilde{\nu}(^2E)$ remains constant, in the mixed diphosphates $(In_{1-x}Cr_x)_4(P_2O_7)_3$ with face-sharing $[M^{III}_2O_9]$ octahedra, a decrease of $\tilde{\nu}(^2E)$ with rising chromium content is found. This result is in agreement with observations for mixed crystals $(Al_{1-x}Cr_x)_2O_3$ and can be understood in terms of partial $\pi$-electron delocalization between adjacent $Cr^{3+}$ ions in the double-octahedra leading to a significant reduction of the interelectronic repulsion for the ions. Here, it is obviously the direct $d_{xy}-d_{xy}$ overlap between two adjacent $Cr^{III}$ atoms that is effective,[33] because the $^4A_{2g} \rightarrow {}^2E_g$ transition in question occurs within the $t_{2g}^3$ ground-state configuration. The cluster geometries in the other structures do not permit such a delocalization. It should also be pointed out that, in the first absorption band, the dip that is related to Fano antiresonance, is much more pronounced for $In_{1-x}Cr_x(PO_3)_3$ than for the other mixed crystal series containing chromium.

The ligand-field parameter $\Delta$ increases with increasing content of the trivalent transition metal for the solid solutions $In_{1-x}Mn_x(PO_3)_3$, $In_{1-x}Cr_x(PO_3)_3$, and $(In_{1-x}Cr_x)PO_4$. As the simplest explanation for this behavior, slightly longer distances $d(M^{3+}-O^{2-})$, due to wider octahedral voids in the indium-rich mixed crystals compared to those in the pure chromium or manganese metaphosphates, might be assumed. Using the changes of $e_{\sigma,max}$ for these three phosphates (Table 2) together with the corelation $e_\sigma(M-O) \approx d(M-O)^{-5}$, one can estimate for the indium-rich members of the solid solutions distances $d(Cr^{3+}-O^{2-})$ and $d(Mn^{3+}-O^{2-})$ that are 0.02 to 0.04 Å, respectively, longer than those in the pure transition-metal phosphates. However, we believe that the explanation is more complex, taking into account the fact that, for the mixed diphosphate series, even a slight decrease of the ligand-field splitting $\Delta$ with increasing chromium content is observed (Table 2, Figure 5). In the latter case, we attribute the decreasing average value of $\Delta$ to more regular $[Cr^{III}O_6]$ octahedra in dimers $[Cr_2O_9]$ than in the unit $[CrInO_9]$. Attractive Cr−Cr interactions compensate to some extent for the electrostatic repulsion between the $Cr^{3+}$ cations, thus leading to less-distorted $[Cr^{III}O_6]$ octahedra. This assumption is supported by a comparison of the M−M and M−O distances for oxides $M_2O_3$ (M = Cr, Al, Ga, In) with the corundum structure, as has already been pointed out by Reinen.[11] As a consequence, the ligand-field-splitting $\Delta$ for the more regular chromophores $[Cr^{III}O_6]$ (with respect to their radial and angular distortion) is slightly smaller than that for the more distorted ones at lower dopant concentration. It is striking that, despite the decreasing polyhedron distortion with increasing $x$(Cr), the splitting of the $\tilde{\nu}_2$ transition (Figure 3b) becomes considerably larger. We think that it is the increasing $\pi$-anisotropy (Table 2, decreasing $e_{\pi,x}/e_{\pi,y}$ ratio) that overcompensates for the size effect. Apparently, for the solid solution $(In_{1-x}Cr_x)_4(P_2O_7)_3$, geometric distortions and electronic anisotropies are counterbalancing effects.

Increasing $x$(Cr) leads to a much more pronounced increase in the splitting of $\tilde{\nu}_2$ (Figure 3c and 5c) in the $(In_{1-x}Cr_x)PO_4$ series than in the diphosphate. In addition, with increasing $x$(Cr), higher values of $\tilde{\nu}_1$, which are a measure for increasing ligand-field splittings $\Delta$, are observed. In accordance with our bonding model, we attribute these effects to increasing $\pi$-anisotropy for the four bridging oxygen ligands (Figure 7c) with increasing $x$(Cr).

The small blue shift of the spin-allowed absorption bands with increasing $x$ for $In_{1-x}Cr_x(PO_3)_3$ can be matched in AO modeling with an increase of $e_{\sigma,max}$ from 7900 to 8300 $cm^{-1}$. Assuming that this shift is related to shorter $d$(Cr−O) distances, one can estimate, on the basis of the relation $e_\sigma(M-O) \approx d(M-O)^{-5}$, a difference in $d$(Cr−O) bond length between pure $Cr(PO_3)_3$ and $In_{0.8}Cr_{0.2}(PO_3)_3$ of only 0.02 Å. Whether this increase of $e_{\sigma,max}$ with increasing $x$(Cr) has a

(33) Reinen, D. *Struct. Bonding* **1969**, *6*, 30.

purely geometric reason cannot be determined. The chromophores $[Cr^{III}O_6]$ in $Cr(PO_3)_3$[32] and anhydrous chromium(III) sulfate $Cr_2(SO_4)_3$[34] show identical average $d$(Cr−O) bond lengths. Therefore, the difference in the observed ligand-field splittings {$\Delta[Cr(PO_3)_3] = 15300\ cm^{-1}$, $\Delta[Cr_2(SO_4)_3] = 14500\ cm^{-1}$ [35]} is quite surprising. However, this observation shows that, even for the same interatomic distances, the related $e_\sigma$ value might be influenced significantly by next-nearest bonding partners.

For manganese(III)-containing compounds with ideal $[MnO_6]$ octahedra, only one spin-allowed transition ($^5E_g \rightarrow {}^5T_{2g}$) is expected. For $d^4$ transition-metal ions, Jahn−Teller distortion produces term splittings, which lead to a larger number of electronic transitions. Therefore, two absorption bands ($\tilde{\nu}_1$ and $\tilde{\nu}_2$ in Figures 3d and 5d), corresponding to the transitions (term symbols given for $D_{4h}$ symmetry) $^5B_{1g} \rightarrow {}^5A_{1g}$ and $^5B_{1g} \rightarrow {}^5B_{2g}$, are observed for all members of the series $In_{1-x}Mn_x(PO_3)_3$. The third transition, $^5B_{1g} \rightarrow {}^5E_g$, is resolved only at high manganese contents as a shoulder of the second absorption band (Figures 3d and 4). As for $In_{1-x}Cr_x(PO_3)_3$, a blue shift of the spin-allowed absorption bands is observed with increasing transition-metal content (Figures 3d and 5d). The change in the color from blue to purple with increasing $x$(Mn) is the result of the higher-energy shift of the second absorption band (from 17200 to 18800 $cm^{-1}$). The shift of $\tilde{\nu}_1$ ($\sim$2220 $cm^{-1}$) with increasing $x$(Mn) is comparatively larger, which is easily explained as an effect of vibronic coupling.

The electronic transition $^5B_{1g} \rightarrow {}^5A_{1g}$ corresponds to excitation of an electron from the $d_{z^2}$-orbital to the $d_{x^2-y^2}$-orbital of $Mn^{3+}$ in a tetragonally elongated octahedral ligand field and is expressed by different values for $e_{\sigma,eq}$ and $e_{\sigma,ax}$ (Table 2): $\tilde{\nu}_1 = 2(e_{\sigma,eq} - e_{\sigma,ax})$, whereas the second transition corresponds to $\tilde{\nu}_2 = 3e_{\sigma,eq} - 4e_{\pi,eq} \approx 2e_{\sigma,eq}$ (because $e_{\sigma,eq} = 4e_{\pi,eq}$). Only an increase of $e_{\pi,eq}$ and a decrease of $e_{\pi,ax}$ can explain the blue shift—larger for $\tilde{\nu}_1$ than for $\tilde{\nu}_2$—in the spectra with increasing $x$(Mn). Apparently, the Jahn−Teller distortion of the $[Mn^{III}O_6]$ chromophores becomes more pronounced with increasing $x$(Mn) (Table 2). As an explanation, improved packing of more strongly distorted octahedra ("cooperative Jahn−Teller-effect"[36]) might be assumed. Figure 8 reports for various polynary manganese(III) fluorides the distortion ($d_{axial} - d_{equatorial}$) of the chromophore $[Mn^{III}O_6]$ in relation to the wavenumber $\tilde{\nu}_1$ of the $^5B_{1g} \rightarrow {}^5A_{1g}$ transition. Data for $Mn(PO_3)_3$ and $In_{0.8}Mn_{0.2}(PO_3)_3$ fit nicely into the general scheme.

This study provides a detailed understanding for the variations of the d-electron energy in various solid solutions. Therefore, additional, not readily explicable features in the spectra of the mixed crystal series $In_{1-x}Cr_x(PO_4)$ (Figure 3c) are particularly puzzling. One reason for the additional absorption bands observed between 8000 and 12500 $cm^{-1}$ might be the presence of small amounts ($\sim$1%) of $Cr^{4+}$ ions in tetrahedral coordination. Studies of the $[Cr^{IV}O_4]$ chromophore showed electronic transitions in the energy range under consideration.[37] However, all attempts to stabilize tetrahedral $[Cr^{IV}O_4]$ chromophores in the more suitable host lattice of quartz-type $FePO_4$ failed, thus indicating the low stability of tetravalent chromium.

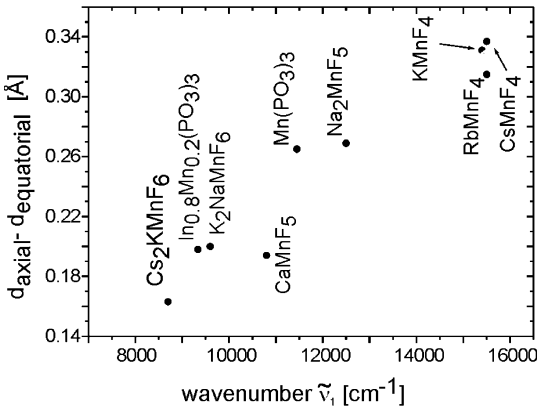


**Figure 8.** Energy of the transition $\tilde{\nu}_1$ ($^5B_{1g} \rightarrow {}^5A_{1g}$) versus the radial distortion ($d_{axial} - d_{equatorial}$) of the chromophore $[Mn^{III}X_6]$ in various fluorides,[39] $Mn(PO_3)_3$, and $In_{0.8}Mn_{0.2}(PO_3)_3$.

## Conclusions

Our study shows that, upon doping of indium phosphates with trivalent chromium or manganese, structural and electronic changes occur that lead to variations of the energies of the d-electronic states of the transition-metal ion. Careful modeling and interpretation of the spectra within the AOM framework allows rather subtle variations in chemical bonding in the solid solutions to be distinguished. The most striking effect upon doping is related to anisotropic $\pi$-bonding between metal d-orbitals and oxygen p-orbitals. Whereas $In^{3+}$ ($d^{10}$ system) shows no d−$\pi$-bonding toward oxygen, the partly filled d-orbitals of $Cr^{3+}$ take part in such interactions. Substituting $Cr^{3+}$ by $In^{3+}$ in the second coordination sphere around a $[Cr^{III}O_6]$ chromophore therefore leads to changes of the $\pi$-bonding in this chromophore. Our study also provides evidence for an "inductive" effect of next-nearest neighbors on the $[Cr^{III}O_6]$ and $[Mn^{III}O_6]$ chromophores. In contrast to these electronic properties, the coordination geometry experiences only small changes due to substitution of $In^{3+}$ by $Cr^{3+}$. Only in the particular case of the solid solution $In_{1-x}Mn_x(PO_3)_3$ do significant geometric changes of the chromophore occur upon doping.

**Acknowledgment.** EDX analyses by Dipl.-Chem. Dirk Worch are gratefully acknowledged. Financial support provided by Deutsche Forschungsgemeinschaft is appreciated. Particular thanks are due to Prof. Dr. D. Reinen (Marburg, Germany) for valuable discussions.

IC061481B

(34) Dahmen, T.; Gruehn, R. *Z. Kristallogr.* **1993**, *204*, 57.
(35) Glaum, R. University of Bonn, Bonn, Germany. Unpublished results, 2004.
(36) Kanamori, J. *J. Appl. Phys.* **1960**, *31*, 14S. Zheng, R. K.; Li, G.; Tang, A. N.; Yang, Y.; Wang, W.; Li, X. G.; Wang, Z. D.; Ku, H. C. *Appl. Phys. Lett.* **2003**, *83* (25), 5250.
(37) Reinen, D.; Rauw, W.; Kesper, U.; Atanasov, M.; Güdel, H. U.; Hazenkamp, M.; Oetliker, U. *J. Alloys Compd.* **1997**, *246*, 193.
(38) Dowty, E. *ATOMS—Program for Crystal Structure Visualization*; Shape Software: Kingsport, TN, 2004.
(39) Köhler, P.; Massa, W.; Reinen, D.; Hofmann, B.; Hoppe, R. *Z. Anorg. Allg. Chem.* **1978**, *446*, 131.